On the chemo-mechanical evolution process of high-volume slag cement paste

Liang, Minfei; Zhang, Yu; He, Shan; Chen, Yu; Schlangen, Erik; Šavija, Branko

DOI
10.1016/j.conbuildmat.2023.132891

Publication date
2023

Document Version
Final published version

Published in
Construction and Building Materials

Construction and Building Materials 400 (2023) 132891

Contents lists available at ScienceDirect

Construction and Building Materials

journal homepage: www.elsevier.com/locate/conbuildmat

On the chemo-mechanical evolution process of high-volume slag cement paste

Minfei Liang, Yu Zhang *, Shan He, Yu Chen, Erik Schlangen, Branko Šavija

Microlab, Faculty of Civil Engineering and Geosciences, Delft University of Technology, Delft 2628, CN, The Netherlands

ARTICLE INFO

Keywords:
Low-carbon cement
High volume slag replacement
Chemo-mechanical properties
Evolution

ABSTRACT

This study investigated the evolution process of high-volume slag cement (HVSC) paste from a chemo-mechanical standpoint. HVSC specimens with a 70 w.t. % slag replacement rate were studied at various ages. Evolution of phase assemblage, microstructure development, and micromechanical properties were analyzed using TGA/XRD/MIP/SEM-EDS and nano-/micro-indentation techniques. A two-scale micromechanical model was built to predict the effective elastic modulus based on the nanoindentation results. Key findings include: 1) Between 7 and 28 days, the formation of calcium silicate hydrate (C-S-H) gel phase improves the effective elastic modulus by filling capillary pores; 2) From 28 to 90 days, the phase assemblage and microstructure remain stable, with a transition from low-density to high-density C-S-H; 3) Between 90 days and 2 years, slag rims produced by slag grains result in increased elastic modulus; 4) The two-scale micromechanical model, combined with nanoindentation data, accurately predicts the effective modulus of HVSC composites, although the unhydrated slag grains-hydrated cement matrix interface may cause an overestimation at an early age. With longer curing time, this interface disappears owing to the continuous hydration of large slag particles and therefore a good match is found between the modelling and experimental results.

1. Introduction

Under the global initiative of reducing carbon dioxide emissions to cope with climate change problems, replacing the energy-intensive ordinary Portland cement (OPC) clinker with industrial by-products like blast furnace slag (*slag* for short) and fly ash is a practical method [1]. The use of slag as a supplementary cementitious material (SCM) in cement and concrete production is a mature application that lasts over a century in Europe and North America [2]. In the Netherlands, cement with about 65 to 70 wt% of slag (CEM III/B) has a market share of about 60% [3]. It is well accepted that the addition of slag brings improvements in various properties of cement paste, including workability, permeability, resistance to chemical attacks (except carbonation), fracture energy, etc. [4].

Blast furnace slag is a by-product of pig iron production, and formed from the combination of limestone fluxes, coke ashes, and residues from iron ore [5]. It can be simplified as a $CaO\text{-}SiO_2\text{-}Al_2O_3\text{-}MgO$ system. In a cement-slag system, the hydration of slag is mainly induced by the OH^- ions (released early by alkali hydroxides, e.g., KOH and NaOH and later by $Ca(OH)_2$) that break down the network structure of slag. The pozzolanic reaction between $Ca(OH)_2$ and slag keeps densifying the microstructure of cement matrix and forming layers of dark rim around unreacted slag particles, resulting in the long-term improvement of mechanical properties of slag cement paste [6]. In the authors' previous study [7], the micromechanical properties of slag rims were characterized and quantified by using a 40-year HVSC specimen. The work in [8] also concluded that the micromechanical properties of slag rims in alkali-activated slag pastes were higher than gel phases in the matrix. This dark rim consists of the 'inner' products of slag, a mixture of C-A-S-H gel phase, and a hydrotalcite-like phase [9–11].

The evolving properties of cementitious materials are intrinsically reflected by the development of phase assemblage and microstructure, which are tractable by a set of techniques e.g., X-ray diffraction (XRD), thermogravimetric analysis (TGA), nuclear magnetic resonance (NMR), scanning electron microscopy (SEM) equipped with energy-dispersive spectrometry (EDS), mercury intrusion porosity (MIP), etc [12]. In the last decades, several studies revealed the evolving phase assemblage and microstructure of slag cement paste using aforementioned techniques.

* Corresponding author.
E-mail addresses: M.Liang-1@tudelft.nl (M. Liang), Y.Zhang-28@tudelft.nl (Y. Zhang), S.He-2@tudelft.nl (S. He), Y.Chen-6@tudelft.nl (Y. Chen), Erik.Schlangen@tudelft.nl (E. Schlangen), B.Savija@tudelft.nl (B. Šavija).

https://doi.org/10.1016/j.conbuildmat.2023.132891
Received 12 February 2023; Received in revised form 26 July 2023; Accepted 6 August 2023
Available online 8 August 2023

Taylor et al. [10] conducted tests of XRD, TGA, NMR, and SEM-EDS on 14-month-old and 20-year-old slag cement samples (with slag content ranging from 0 to 100% wt.) to understand the evolution process of hydration products, regarding morphology, Ca/Si atomic ratio, aluminosilicate chain length of C-A-S-H gel phase, as well as Mg/Al atomic ratio of hydrotalcite-like phase. Based on XRD and SEM-EDS, Escalante-Garcia et al. [13] characterized the hydration products of 1-year-old slag cement samples which contained 60% wt. slag cured at temperatures ranging from 10 to 60 °C. According to stoichiometric calculations, Chen et al. [6] proposed a reaction model for slag cement to correlate the composition of raw materials (including cement and slag) with the quantities and composition of hydration products at different curing ages. In addition, some important indices, e.g., hydration degree of slag, chemically bound water content, and calcium hydroxide content, are often measured by tests like XRD, TGA, SEM, etc. [8,14]. In recent years, studies on the hydration of slag cement paste have been concentrated on more refined factors, such as the slag reactivity of different Mg/ Al ratios [15], and the influence of alumina [16] and sulfur [17] on the early-age hydration.

Accompanying the evolution of various hydration products, the micromechanical properties of different phases evolve accordingly with time, which is important for understanding the overall mechanical performance of the material. Nanoindentation is often used to measure the indentation modulus and hardness of different phases in cementitious materials, including low-density C-S-H (LD C-S-H), high-density C-S-H (HD C-S-H), unhydrated particles, etc. [18,19]. Furthermore, multiscale models - either FEM methods (e.g., the Delft Lattice Model [20]) or micromechanical homogenization schemes (e.g., Mori- Tanaka or Self-consistent scheme [21]) - allow predicting the overall mechanical performance such as elastic modulus based on nanoindentation results. Note that the number of studies concentrating on the micromechanical properties of cement-slag system is much lower than those focusing on OPC systems. Wei et al. [22] conducted nanoindentation tests on slag cement paste with a slag content of 70% wt. and w/c of 0.30. By schematizing the sample as a three-phase material and calculating the volume fraction of each phase through backscattered electron (BSE) images, the authors upscaled the micromechanical properties of each phase measured by nanoindentation to the overall mechanical properties of the composites using the Self-Consistent method. Šavija et al. [23] built a microscale lattice model for predicting the overall mechanical properties of slag cement at 28 days. By correlating the elastic modulus measured by nanoindentation tests with the grayscale values of X-ray computed tomography (XCT), a phase-free micromechanical model with a continuous distribution of micromechanical properties was built to predict the elastic modulus and tensile strength of the material.

To sum up, the aforementioned studies encompass the phase assemblage, microstructure, and micromechanical properties of cement-slag system at different designated ages, forming a systematic understanding of the composite. However, most investigations concentrated either at chemical measurement or micromechanical characterization, thus leading to a lack of mutual verification between the two. Additionally, to examine the micromechanical properties of slag cement mixture, specimens were typically cured up to 28 days. Evolution of slag cement pastes remains scarcely studied. Meanwhile, only a small fraction of slag hydrates at this stage (i.e., until 28 days) due to its relatively low reaction rate, and its influence cannot be manifested completely. Besides, it is commonly recognized that the improvement in long-term mechanical properties of slag cement paste can be ascribed to the continuous densification of microstructure, originating from the pozzolanic reaction between portlandite and slag. It is still unknown whether other factors also contribute to this improvement. To address these issues, a chemo-mechanical study on cement-slag system with a continuous curing period up to later age (ie., years) is essential.

Therefore, the current study conducted experiments on high-volume slag cement (HVSC) paste (70% wt. replacement level) at the age of 7-day, 28-day, 90-day, and 2-year. The experimental results of around 40-year-old HVSC sample from the authors' previous study [7] would also be used for discussion. Note that a reactive slag and a high substitution level were employed in the study to amplify the influence of slag itself. Tests including TGA/ XRD/ MIP/ SEM-EDS were conducted to characterize the evolution of phase assemblage and microstructure of the HVSC paste samples. Furthermore, nanoindentation and microindentation measurements were carried out to derive the evolution process of local and overall micromechanical properties. Afterwards, a two-scale micromechanical model was built to upscale the micromechanical properties of individual phases to HVSC paste. Phase assemblage evolution and microstructure development explained well the observations in the micromechanical tests. An in-depth understanding of the chemo-mechanical evolution process of HVSC was thus provided. Moreover, a new assumption concerning the evolution/ densification of the transitional areas between unhydrated slag particles and cement matrix was proposed.

2. Experimental

2.1. Materials

CEM I 42.5 N manufactured by the ENCI Maastricht B.V. and a reactive slag with high MgO content (For detailed information, please refer to [15].) were used as the cementitious materials. The chemical compositions of the cementitious materials are shown in Table 1. The slag substitution level was set as 70% wt., to simulate CEM III/B that has been widely used in the Netherlands. A commonly-used water-binder ratio of 0.40 was adopted. Raw materials including cement and slag were firstly mixed for 1 min in the mixer. After adding water, they were continuously mixed for another 2 min. Cylindrical specimens with a radius of 1.3 cm and a height of 3 cm were casted for each sampling age of 7 days, 28 days, 90 days, and 2 years. All specimens were sealed at room temperature of 20 ± 3 °C.

2.2. Characterization of phase assemblage and microstructure

To reveal the evolution process of phase assemblage and microstructure, tests including TGA, XRD, MIP, SEM- EDS were conducted on the 7-day, 28-day, 90-day, and 2-year HVSC paste specimens. Before the tests, slices cut from the corresponding specimens were immersed in the isopropanol solution for one week to stop hydration [24]. Subsequently, the slices were crushed and ground to a grain size below 63 μm for TGA and XRD measurements.

XRD tests were carried out on a Philips PW 1830/40 powder diffractometer using the Cu K-alpha radiation. The adopted acceleration voltage was 40 kV and the X-ray beam current was 40 mA. The XRD data was collected with a step size of 0.03° for a 2θ range from 5° to 60°. TGA test was performed on Netzsch STA 449 F3 Jupiter under Argon atmosphere. Around 40 mg of the sample powder was heated up from 40 to 900 °C with a heating rate of 10 °C/minute in an Al_2O_3 crucible, with an identical crucible as reference.

MIP analysis was used to measure the critical pore size distribution and porosity of HVSC pastes at different ages. Specimens were crushed into small pieces (with a size typically smaller than 4 mm) and stored in a vacuum container to remove isopropanol from the pores. The intrusion process of the mercury was performed in the following steps: 1) a low-press state from 0 to 0.170 MPa; 2) a high-pressure state from 0.170 to 210 MPa; 3) an unpressurized state from 210 to 0.170 MPa. The pore radius was calculated based on the Washburn equation, with the surface tension of mercury being 0.485 N/m and the contact angle between mercury and sample being 140° [25].

SEM-EDS was employed to observe the elemental compositions of main hydration products, i.e., C-A-S-H gel phase and hydrotalcite-like phase of the HVSC pastes with time. The sample preparation procedures for SEM-EDS analysis are the same as the micromechanical tests and will be introduced in Section 2.3. Samples were carbon coated before

Table 1
Chemical compositions of the adopted cementitious materials (% wt.).

	CaO	SiO_2	Al_2O_3	MgO	FeO/Fe_2O_3	TiO_2	MnO/Mn_2O_3	Na_2O	K_2O	SO_3	Residual
Cement	64.0	20.0	5.0	–	3.0	–	–	0.58	–	2.93	4.49
Slag	34.09	32.99	15.01	16.07	0.34	0.73	0.16	0.22	0.21	0.01	0.13

being moved into an FEI QUANTA FEG 650 ESEM. An accelerating voltage of 10 kV and a working distance of 10 mm were used throughout the research. Approximately 100 points were selected for each sample to characterize the composition of hydration products.

2.3. Micromechanical tests

2.3.1. Sample preparation

Nanoindentation and microindentation tests were carried out to probe the local and overall micromechanical properties of the HVSC pastes at different ages. A KLA G200 nanoindenter equipped with an XP head and DCM II head was used to conduct the micromechanical tests. Before the measurements, the roughness of the sample surface needs to be small enough to fulfil the assumption of an ideally flat surface in the calculation of indentation modulus, either based on root-mean-squared (RMS) roughness or a mirror-like surface [26]. The following procedure was used to obtain the flat surface for nanoindentation and microindentation tests: 1) immerse the sample in isopropanol solution to arrest hydration; 2) slice the sample into a thin slice (around 2 mm thick) using a micro-dicing saw; 3) grind the sample using a 4000 grit abrasive paper for 5 min; 4) polish the sample with synthetic silk polishing cloth (MD-Dac from Struers) charged with 3 μm and 1 μm diamond pastes for 2 separate 30-minute sessions. During the grinding and polishing processes, an oil-based lubricant (DP-Lubricant Brown from Struers) was used to dissipate the heat build-up. Between each grinding and polishing interval, the sample was immersed in an ultrasonic bath filled with pure ethanol for 30 sec to remove debris. According to the roughness criterion proposed by [26], the measurement of surface roughness highly depends on the chosen scan size, the inhomogeneity of sample surface, and the filtering parameters, thus, the surface roughness can only be regarded as a qualitative or comparative index for evaluating the validity of the surface preparation. Meanwhile, a more conservative rule-of-thumb is a mirror-like surface able to reflect overhead light. The surface of HVSC paste sample in Fig. 1, which shows that the sample was well polished to qualify for a mirror-like surface. Based on a digital microscope (Keyence VHX-7000), the roughness (i.e., arithmetical mean height) of the center area of 400 × 500 μm^2 for the samples at 7-day, 28-day, 90-day and 2-year were calculated to be less than 80 nm using a Gaussian filter (i.e., a S-filter of 20 μm and a L filter of 25 μm).

Fig. 1. Mirror-like surface reflecting overhead circular light.

2.3.2. Testing details

The nanoindentation and microindentation tests were performed using DCM II head and XP head, respectively. Both the DCM II head and XP head were first calibrated by the standard SiO_2 with an elastic modulus of 72 GPa. The nanoindentation tests aim to measure the local micromechanical properties using Continuous Stiffness Measurement (CSM) [27,28]. By imposing a small oscillation with an amplitude of 1 nm and a frequency of 75 Hz on the primary loading signal, the elastic modulus can be measured continuously throughout the indentation depth, which is set as 500 nm in this study. For each HVSC paste sample, 20 × 30 indents were made with a spacing of 10 μm. A typical load–displacement curve and continuous measurement of the elastic modulus of the 2-year sample are shown in Fig. 2. It should be noted that the nanoindentation results at a depth of h actually represent the local micromechanical properties of the surrounding composites with a length scale of 3–5 h [18,29]. Aiming to probe the micromechanical properties of a single phase, the indentation depth should be properly selected. Published studies [22,30] have found that an indentation depth of 100–200 nm is considered to be deep enough for HD C-S-H, while LD C-S-H requires a deeper indentation depth of around 500 nm. Therefore, in this study, the value of elastic modulus is calculated by taking the average of the CSM results at the depth ranging from 100 to 500 nm.

Microindentation tests were conducted with a load-controlled method: the load applied on the sample was increased to the maximum (i.e., 3500 mN in this study) in 30 sec, kept for 10 sec, and then decreased to 10% of the maximum load in another 30 sec. The displacement into the surface, which reaches over 15000 nm, is sufficient to represent the overall micromechanical properties of the designated HVSC paste sample at certain ages [31]. Typical load–displacement curves of the investigated HVSC paste samples are shown in Fig. 3.

The indentation modulus was calculated based on the slope at the onset of the unloading region of the load–displacement curve [32,33]:

$$E_r = \frac{dP}{dh} = \frac{\sqrt{\pi}}{2\beta}\frac{S}{\sqrt{A_c}} \tag{1}$$

where E_r is the indentation modulus; S is the contact stiffness calculated at the beginning portion of the unloading curve; A_c is the projected area of the indenter which is calculated using the calibration parameters derived by a standard SiO_2 sample; β is the geometry constant of the Berkovich tip which equals to 1.034. For a homogenous isotropic elastic material, the indentation modulus E_r can be correlated to the elastic modulus E and the Poisson's ratio ν of the local material, as follows:

$$\frac{1}{E_r} = \frac{1-\nu^2}{E} + \frac{1-\nu_i^2}{E_i} \tag{2}$$

where E_i and ν_i are the elastic modulus and Poisson's ratios which are equal to 1141 GPa and 0.07, respectively. The Poisson's ratio of all samples is assumed to be 0.20. Despite that the accurate value of Poisson's ratio of cement paste is not accurately known, it only has a minor influence on the calculated elastic modulus: a change in Poisson's ratio over the full range of possible/reasonable values (that is from 0.18 to 0.25), reduces the computed value of elastic modulus by only about 7 percent [18,34].

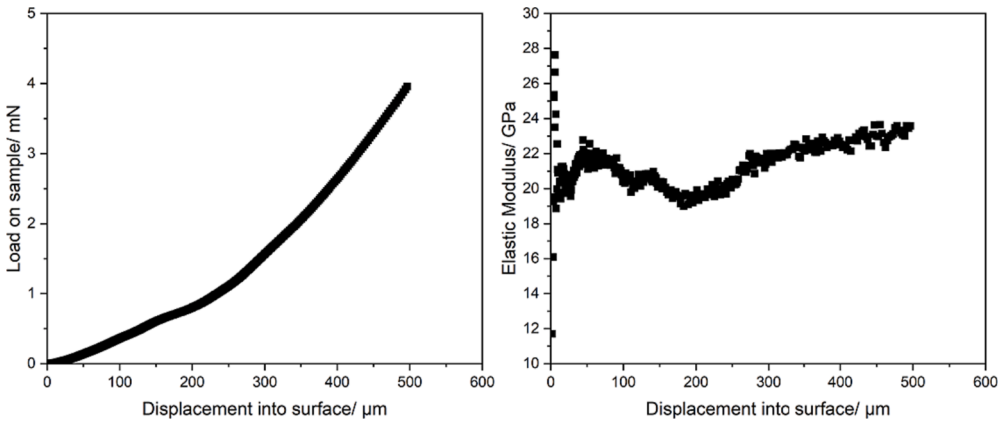

Fig. 2. Load-displacement curve and the CSM test results of one typical indent from the 2-year sample.

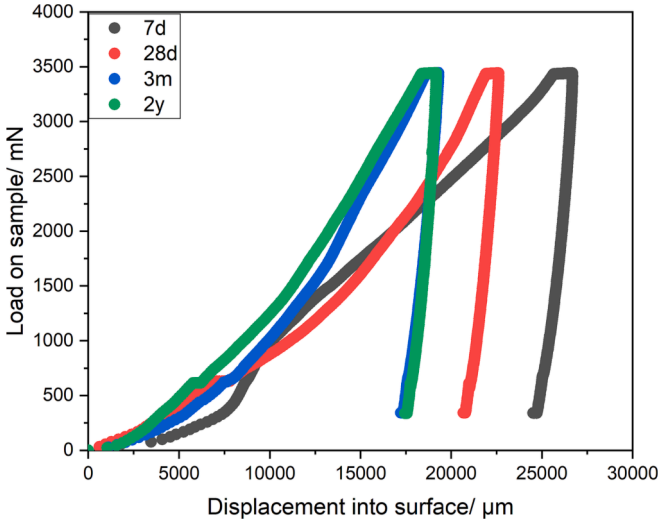

Fig. 3. Load-displacement curves of microindentation tests for these four investigated samples.

2.3.3. Gaussian mixture model (GMM) for statistical analysis

During the nanoindentation test, each indent measures the micromechanical properties of a composite of the characteristic length 1.5 ~ 2.5 μm when the maximum indentation depth is 500 nm [18]. Therefore, the nanoindentation results over a grid (i.e., 20 × 30 in this study) follow a continuous distribution distinguished by several peaks which are representative of certain phases. Assuming that: 1) the distribution of micromechanical properties of a composite dominated by a certain phase follows the Gaussian distribution; and 2) the superposition of the distribution of each phase is linear, then the GMM is suitable to decompose the distribution of each phase from the overall histogram of grid indentation results [35,36]. In the GMM model, the overall distribution of testing results (X) can be expressed as the weighted sum of the distribution of multiple phases X_i ($i = 1, 2, 3, \ldots, N$), as follows:

$$p\left(X|\left\{w,\mu,\sigma^2\right\}\right)=\sum_{i=1}^{N} w_i p\left(X_i|\left\{\mu_i,\sigma_i^2\right\}\right) \tag{3}$$

where w_i, μ_i, σ_i are the fraction, mean, and standard deviation of i-th phase, respectively. The probabilistic distribution X_i is a Gaussian distribution and, therefore, is solely determined by its mean and standard deviation, as follows:

$$p\left(X_i|\left\{\mu_j,\sigma_j^2\right\}\right)=\frac{1}{\sqrt{2\pi\sigma_i^2}}exp\left(\frac{(X_i-\mu_i)^2}{2\sigma_i^2}\right) \tag{4}$$

2.3.4. Micromechanical homogenization schemes

Micromechanics links the mechanical properties of individual phases to the effective mechanical properties of the composite. The effectiveness of homogenization schemes including Mori-Tanaka (M-T) [37] and Self-Consistent (SC) [38] in predicting the effective mechanical properties of cement composites from micromechanical properties of individual phases has been proven by numerous studies [18,39–41]. Herein, a two-scale micromechanical model (Fig. 4) was built, assuming the HVSC paste as a five-phase composite. The first four phases are solid components of different hydration products, slag, and cement clinker, which are distinguished by their mechanical properties according to the results of statistical nanoindentation tests (see Section 3.2). The fifth phase comprises large pores which cannot be directly measured by nanoindentation tests; instead, their volume fraction is determined by BSE images. The MT scheme is suitable for the case where the matrix with a relatively large volume encloses the inclusion phase [37], while the SC scheme is suitable for the case where the matrix and the inclusion are difficult to distinguish and are both wrapped in a homogeneous medium [38]. In level 1, phases 1 and 2 correspond to the main hydration products and form a clear inclusion-matrix morphology, with phase 1 (i.e., LD C-S-H) being the matrix and phase 2 (i.e., HD C-S-H) being the inclusion. Therefore, the MT scheme is adopted to homogenize Phase 1 and 2. Then, the homogenization result of the level 1 is used as the input of the matrix for Level 2, where different inclusions, including Phase 3 and 4 (mainly CH, slag and cement clinker), are presented. Therefore, in level 2, the SC scheme is adopted to obtain the effective elastic modulus of the HVSC paste.

In a linear elastic regime, following continuum micromechanics, the microscopic strain can be linked to the macroscopic strain through the following localization relations:

$$\boldsymbol{\varepsilon}_i = \boldsymbol{A}_i : \boldsymbol{E} \tag{5}$$

where i corresponds to the i-th phase; $\boldsymbol{\varepsilon}$ is the local strain; $\boldsymbol{E}$ is the macroscopic strain; $\boldsymbol{A}$ is the fourth-order localization tensor which concentrates a macroscopic quantity prescribed at the boundary into a microscopic phase. The macroscopic strain $\boldsymbol{E}$ and stress $\boldsymbol{\Sigma}$ of a representative elementary volume (REV) V_R is the volume average of the microscopic strain $\boldsymbol{\varepsilon(x)}$ and stress $\boldsymbol{\sigma(x)}$ as below:

$$\boldsymbol{E}=\langle\boldsymbol{\varepsilon}(\boldsymbol{x})\rangle_{V_R}=\frac{1}{V_R}\int\boldsymbol{\varepsilon}(\boldsymbol{x})dV=\sum_{i=1}^{n} w_i\langle\boldsymbol{\varepsilon}(\boldsymbol{x})\rangle_{V_i} \tag{6}$$

$$\boldsymbol{\Sigma}=\langle\boldsymbol{\sigma}(\boldsymbol{x})\rangle_{V_R}=\frac{1}{V_R}\int\boldsymbol{\sigma}(\boldsymbol{x})dV=\sum_{i=1}^{n} w_i\langle\boldsymbol{\sigma}(\boldsymbol{x})\rangle_{V_i} \tag{7}$$

where w_i is the volume fraction of each phase, as determined by the statistical nanoindentation tests in Section 3.2; $\boldsymbol{x}$ is the position vector; n

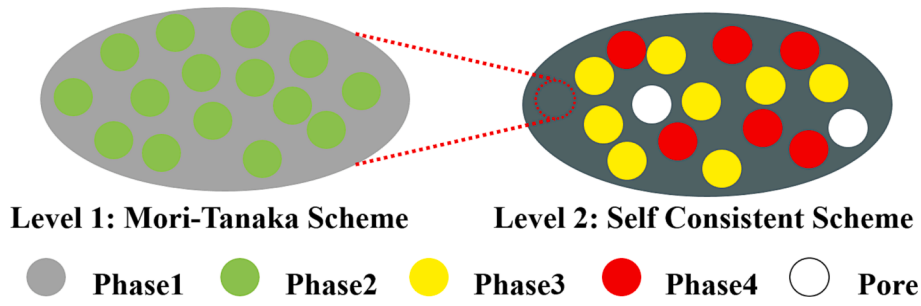

Fig. 4. The two-scale micromechanical model of HVSC paste.

is the number of phases. Substituting Eq. (6) into Eq. (5), one can get:

$$\sum_{i=0}^{n} w_i \boldsymbol{A_i} = \boldsymbol{I} \tag{8}$$

where $\boldsymbol{I}$ is the fourth-order identity tensor. With a linear elastic constitutive relationship, the Eq. (7) can be rewritten as:

$$\boldsymbol{\Sigma} = \frac{1}{V_R}\int \boldsymbol{C}(\boldsymbol{x}) : \boldsymbol{\varepsilon}(\boldsymbol{x}) dV = \sum_{i=1}^{n} w_i \boldsymbol{C_i} \langle \boldsymbol{\varepsilon}(\boldsymbol{x}) \rangle_{V_i} = \sum_{i=1}^{n} w_i \boldsymbol{C_i} : \boldsymbol{A_i} : \boldsymbol{E} \tag{9}$$

where $\boldsymbol{C_i}$ is the stiffness tensor of i-th phase. Therefore, the effective stiffness tensor $\boldsymbol{C_{eff}}$ of the material can be expressed as:

$$\boldsymbol{C_{eff}} = \sum_{i=1}^{n} w_i \boldsymbol{C_i} : \boldsymbol{A_i} \tag{10}$$

For the M-T scheme, the localization tensor for i-th inclusion phase can be expressed as:

$$\boldsymbol{A_i} = \boldsymbol{A_i}^{\boldsymbol{MT}} : [\sum_{i=0}^{n} w_i \boldsymbol{A_i}^{\boldsymbol{MT}}]^{-1} \tag{11}$$

$$\boldsymbol{A_i}^{\boldsymbol{MT}} = [\boldsymbol{I} + \boldsymbol{S_i^0}(\boldsymbol{C_i} - \boldsymbol{C_0})]^{-1} \tag{12}$$

where the $\boldsymbol{S_i^0}$ is a fourth-order tensor called Hill polarization tensor, which is related to the elastic properties of the matrix and the geometry of the i-th inclusion [42]; $\boldsymbol{C_0}$ is the stiffness tensor of the matrix phase. The localization tensor of the matrix phase can further be obtained by Eq. (8). Assuming a spherical inclusion and substituting Eq. (11–12) into Eq. (10), the homogenized bulk and shear moduli can be obtained as follows:

$$k_{eff} = \frac{\sum_{i=1}^{n} w_i k_i \left(1 + \alpha_0 \left(\frac{k_i}{k_0} - 1\right)\right)^{-1}}{\sum_{i=1}^{n} w_i \left(1 + \alpha_0 \left(\frac{k_i}{k_0} - 1\right)\right)^{-1}} \tag{13a}$$

$$\mu_{eff} = \frac{\sum_{i=1}^{n} w_i \mu_i \left(1 + \beta_0 \left(\frac{\mu_i}{\mu_0} - 1\right)\right)^{-1}}{\sum_{i=1}^{n} w_i \left(1 + \beta_0 \left(\frac{\mu_i}{\mu_0} - 1\right)\right)^{-1}} \tag{13b}$$

$$\alpha_0 = \frac{3k_0}{3k_0 + 4\mu_0} \tag{13c}$$

$$\beta_0 = \frac{6k_0 + 12\mu_0}{15k_0 + 20\mu_0} \tag{13d}$$

where k and μ are the bulk moduli and shear moduli; the subscript i and 0 represent i-th inclusion and matrix, respectively. Therefore, the effective elastic modulus of the composite can be expressed as:

$$E_{eff} = \frac{9k_{eff}\mu_{eff}}{3k_{eff} + \mu_{eff}} \tag{14}$$

For the SC scheme, the localization tensor for i-th phase can be expressed as:

$$\boldsymbol{A_i} = [\boldsymbol{I} + \boldsymbol{S_i^{eff}}(\boldsymbol{C_i} - \boldsymbol{C_{eff}})]^{-1} \tag{15}$$

In the SC scheme, the localization tensor $\boldsymbol{A_i}$ is dependent on the effective stiffness tensor $\boldsymbol{C_{eff}}$, which needs to be calculated iteratively based on Eq. (10) and Eq. (15).

3. Results

3.1. Hydration products

In this section, the results of TGA, XRD, SEM-EDS of HVSC samples at 7-days, 28-days, 90-days and 2-years will be presented. These results are analyzed and summarized in the following three stages: Stage I: 7-day to 28-day; Stage II: 28-day to 90-day; and Stage III: 90-day to 2-year based on the sampling schedules.

3.1.1. TGA

The TGA results are shown in Fig. 5, where the differential thermogravimetric (DTG) results are also presented. The peaks of DTG curves at around 125, 175 (and 300), 225 as well as 400, and 450 °C correspond to C-A-S-H gel phase [12], calcium monosulfoaluminate (*monosulfate* for short), hydrotalcite-like phase [43,44], and portlandite, respectively. Also, these results show a clear evolution process of hydration products: From 7-days to 2-years, the amounts of C-A-S-H gel phase and hydrotalcite-like phase increase, while the content of portlandite decreases. In stage I (7-days to 28-days), which is mainly dominated by the hydration of cement clinkers, the highest increment of C-A-S-H gel phase can be seen. For stage II (28-days to 90-days), minor changes are detected, and the TG curves almost overlap. As for stage III

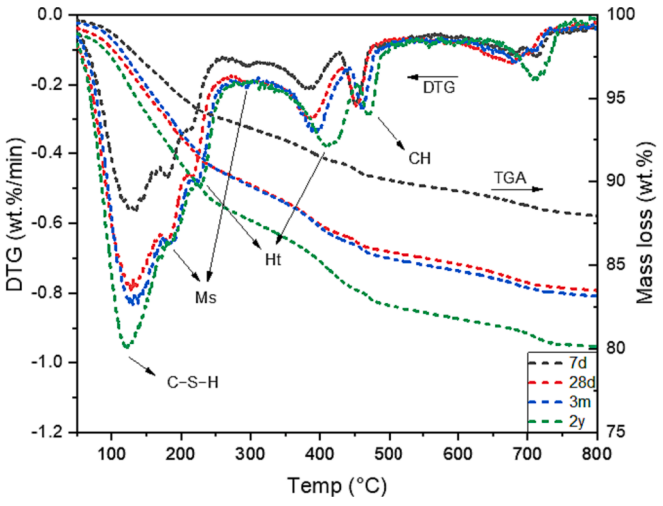

Fig. 5. TGA and DTG results of HVSC samples at 7-day, 28-day, 90-day and 2-year CH: portlandite; Ht: hydrotalcite-like phase; Ms: monosulfate.

(90-days to 2-years), a significant increase in hydrotalcite-like phase is observed, indicating a continuous pozzolanic reaction between slag and portlandite.

3.1.2. XRD

The XRD scans of these samples are shown in Fig. 6. Within the range of 8 to 20° (2θ), the peaks of monosulfate, hydrotalcite-like phase, and portlandite can be clearly seen. The main peak for C-A-S-H phase, located at ~30° (2θ), is difficult to distinguish from that of alite (C_3S), and therefore it is not displayed here. The following can be observed: 1) the consumption of portlandite is continuous, indicated by the decreasing peak intensity located at ~18° (2θ) over time; 2) a significant increase of hydrotalcite-like phase happens in Stage III (90-day to 2-year), in agreement with the TGA results shown in Fig. 5.

3.1.3. SEM-EDS

In order to better trace the evolution of phase assemblage, C-A-S-H gel phase and hydrotalcite-like phase in particular, SEM-EDS was also conducted on cement matrix and slag rims, respectively. As shown in Fig. 7(a), the determined Ca/Si atomic ratio of C-A-S-H gel phase decreased continuously over time (especially during Stage III), from ~1.3 at 7 days to ~1.0 after 2 years of hydration, according to the method put forward in [45,46]. Due to the reduction of Ca/Si ratio, the chain length of the gel phase increased correspondingly [45], which suggested the maturity or evolution of C-A-S-H with time. The scatter plot of Mg/Si against Al/Si in atomic ratio is shown in Fig. 7(b). Before 90-days (Stages I and II), the Mg/Si and Al/Si ratios (see Fig. 7(b)) of

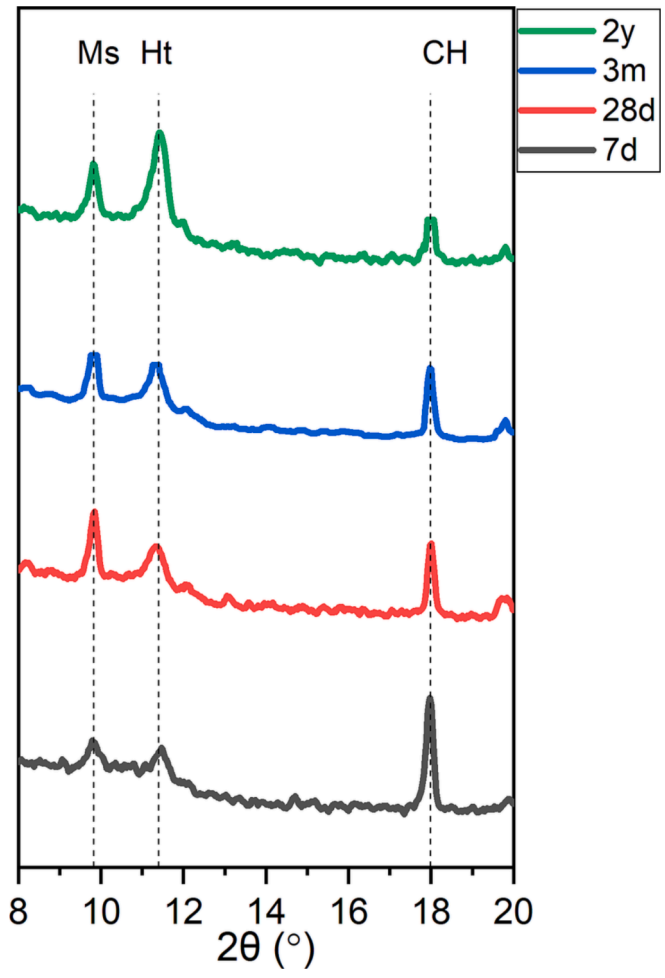

Fig. 6. XRD results of HVSC samples at 7-day, 28-day, 90-day and 2-year CH: portlandite; Ht: hydrotalcite-like phase; Ms: monosulfate.

'inner' products in slag rims are mostly less than 1.0 and 0.6, respectively, indicating a low hydration degree of slag. In comparison, for HVSC sample at the end of Stage III, Mg/Si and Al/Si ratios fluctuate in the range of 1.0 to 4.0 and 0.6 to 1.8, respectively, suggesting that a much higher slag hydration degree is achieved at this age, and hydrotalcite-like phase dominates in the rims of unhydrated slag particles. It is consistent with the results obtained through TGA (Fig. 5) and XRD (Fig. 6), where a considerable increment in hydrotalcite-like phase content is detected after Stage III. Additionally, note that the Mg/Al atomic ratio of hydrotalcite-like phase (obtained from the slope of regression line fitting these scattering points) remains stable with curing.

3.2. Microstructure

3.2.1. SEM-BSE

Fig. 8 shows the typical BSE images of HVSC paste samples at different ages with a magnification of 2000 ×. Unhydrated cement grains, appearing as the lightest part, (e.g., circled and labelled 1 in Fig. 8(a) and (d)) are still observed even at 2 years. Monosulfate appeared as widespread, fine and compact clusters intermixed with the cement matrix (e.g., circled and labelled 2 Fig. 8(a)). Hydrates, precipitated as rims around unreacted slag grains, are connected with the surrounding matrix from 28 days as shown in Fig. 8(b). In addition, BSE images clearly demonstrate a reduction in porosity with curing time: the microstructure of HVSC paste sample is porous at 7 days; however, the continuous hydration of cement clinkers results in the densification of cement matrix at 28 days (Fig. 8(b)). During Stage III (90-day to 2-year), clear dark grey rims appear surrounding unreacted slag grains (i.e., slag rims), which are rich in hydrotalcite-like phase. In addition, fully-hydrated slag particles can also be frequently observed across the matrix, indicating a notably higher hydration degree of slag at this age.

3.2.2. MIP

MIP results are shown in Fig. 9. As seen in the graph, the critical pore diameter [12] shifts left continuously with time, due to the pozzolanic reaction between slag and portlandite. The hydration products keep densifying the microstructure; as a result, the porosity of HVSC paste decreases with the extension of curing period following the order: 2-year≪ 90-day less than 28-day≪ 7d. Note, however, that the porosity of HVSC paste at 28 and 90 days is very similar. Fig. 10 displays the proportions of different types of pores in HVSC pastes based on the classification proposed in [47], i.e., less than 10 nm for gel pore, 10–500 nm for small capillary pore, 500–1000 nm for medium capillary pore, and > 1000 nm for large capillary pore. For the calculation of pore diameter, the Washburn equation explains the relationship between pore diameter (D) and pressure (P) as the below formula shows,

$$P = -\frac{4\gamma cos(\theta)}{D} \tag{16}$$

of which the surface tension of mercury (γ) is 0.485 N/m at 25 °C and the contact angle between mercury and sample (θ) is 140°. As can be seen, the percentages of capillary pores decrease with curing time while the proportion of gel pores increases.

3.3. Micromechanical properties

The histogram of elastic modulus of nanoindentation and the corresponding deconvolution results based on the GMM model are shown in Fig. 11. With a loading depth of 500 nm, the result of each indent reflects the micromechanical response of the surrounding composites with a length scale of 1.5 ~ 2.5 μm, and therefore can be considered as an index of local mechanical properties [18]. By fitting the histogram of nanoindentation results with the GMM model, the distribution of each phase in the HVSC composite can be obtained and represented with an

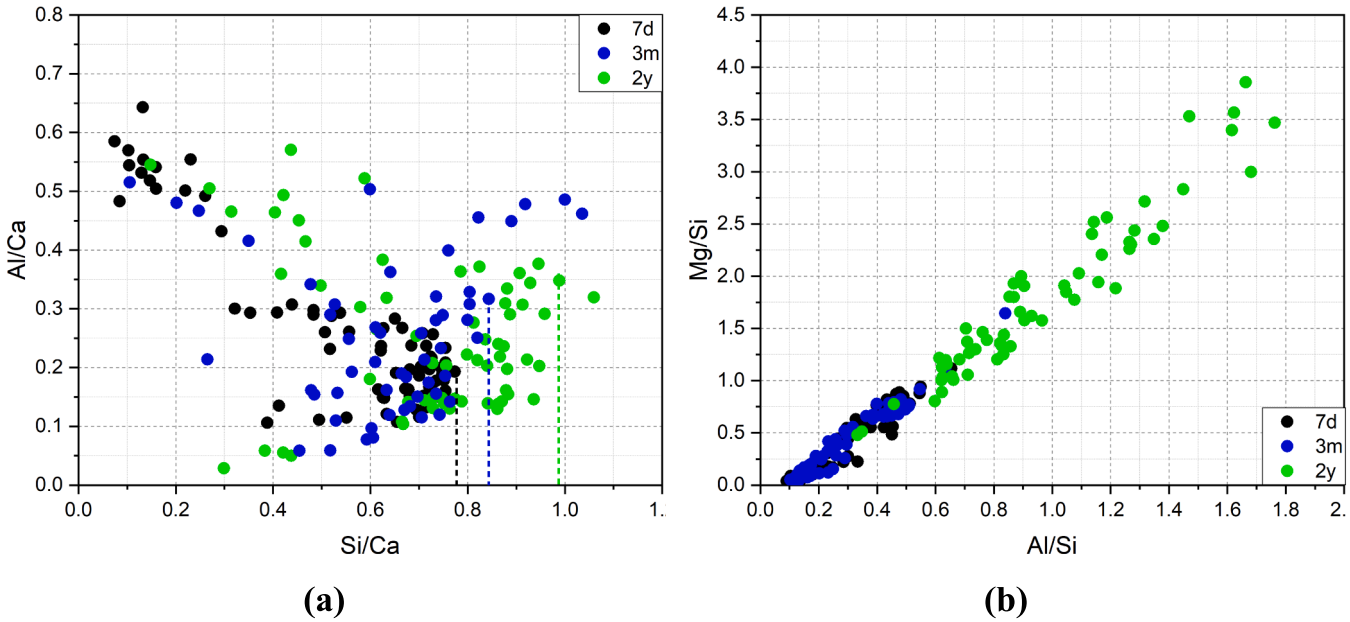

Fig. 7. Scatter plot in atomic ratio of (a) Al/Ca vs. Si/Ca on cement matrix; and (b) Mg/Si vs. Al/Si on slag rim.

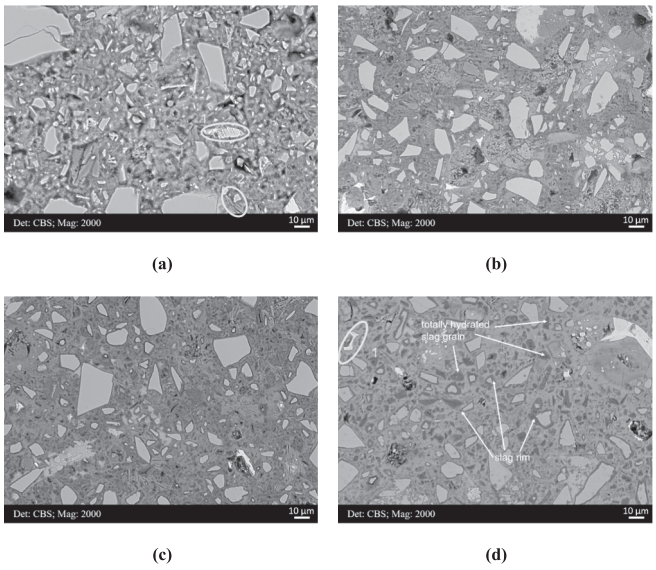

Fig. 8. Typical BSE images of HVSC samples at the ages of (a) 7-days; (b) 28-days; (c) 90-days; (d) 2-years.

independent Gaussian distribution solely dependent on the fraction w_i, mean μ_i, and variance σ_i, with $i = 1, 2, 3, 4$ standing for four different phases in the HVSC samples. The following can be seen in the graphs:

1) For HVSC pastes throughout the investigated ages, the sum of the first two phases ($i = 1, 2$) is 75%, 74%, 76%, and 82%, and is most likely to be the major hydration products, i.e., LD C-S-H and HD C-S-H [48]. Although the volume fraction determined by the deconvolution method is not as precise as that determined by BSE image analysis [49], the overall trend still presents a continuous increase of hydration products with time, especially at Stage III (90-days to 2-years), which is consistent with the results in Section 3.1.
2) The third and fourth phases ($i = 3, 4$) represent two mixed phases with high variance σ_i. The third phase ($i = 3$) is a mixture of HD C-S-H, portlandite, and unhydrated slag particles, and the fourth phase ($i = 4$) is a mixture of unhydrated slag grains and cement clinkers. Except for the complexity of phase composition, another reason accounting for the high variance of these two composites lies in their low fractions, which may require more indents to better quantify the micromechanical properties.
3) At 7-days, 28-days, and 90-days, the mean of the elastic modulus of the first phase ($i = 1$) increases from 12.26 to 15.42 and then 19.30 GPa, indicating a continuous pore-filling process. During Stage II (28-day to 90-day), the percentage of the second phase ($i = 2$) increases from 30 to 43%, suggesting a transformation from LD- C-S-H to HD C-S-H. At 90-days, the first two phases ($i = 1, 2$) coincide and become a single phase. Recently, He et al. [50] have also confirmed that the continuous generation of C-A-S-H contributes to the densification of outer products, resulting in the improvement of the elastic modulus of outer products, and narrowing the gap between the elastic modulus of inner products and the outer products with longer curing age.
4) During Stage III (90-days to 2-years), a new second phase ($i = 2$) appears and distinguishes itself from the first one with a higher mean elastic modulus. This phase represents the component of slag rim, which was directly tested by the authors in their previous study [7]. One should keep in mind that this phase is a mixture of a C-A-S-H gel phase and a hydrotalcite-like phase. This will be discussed in detail in Section 4.1.

To summarize, based on the nanoindentation results, four (mixed) phases distinguished by their differences in micromechanical properties can be obtained and their compositions can be speculated according to widely-accepted nanoindentation results of specific hydration products, slag and clinkers in the published literatures [7,22,39,48] (Table 2).

In the microindentation test (i.e., with a loading depth over 15 μm), the micromechanical properties with a characteristic length over 45 ~ 75 μm were tested and considered as the effective mechanical properties of the HVSC paste [31,51,52]. For each age, 10 micro indents were made. In addition, the two-scale micromechanical model introduced in Section 2.3.4 was used to calculate the effective elastic modulus by taking the mean value and volume fraction of each of the four (mixed) phases derived by the statistical nanoindentation. It should be stressed that the deconvolution results of statistical nanoindentation distinguish the four phases by their difference in stiffness, not on the potential mineral phases. The mean value of elastic modulus of each phase

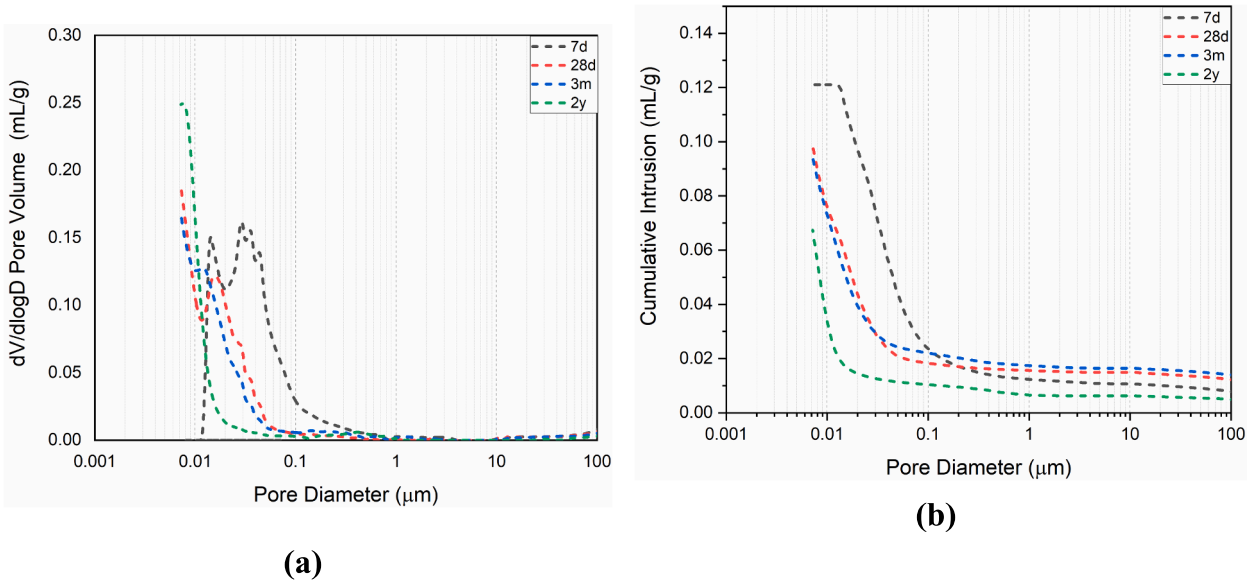

Fig. 9. MIP results of HVSC samples: (a) pore size distribution; and (b) cumulative volume of mercury intrusion.

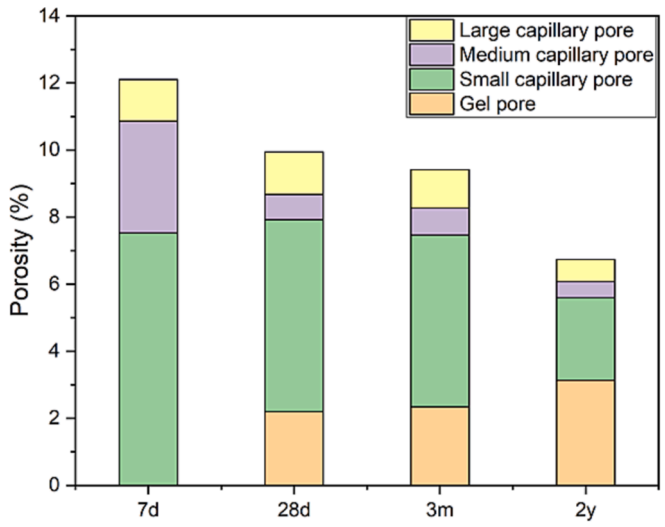

Fig. 10. The proportions of different types of pores in HVSC samples at different ages.

derived by nanoindentation does not necessarily represent a pure phase that contains only a single type of hydration product, unhydrated slag particle or cement clinker, especially for phase 3 and 4 which are always composites of CH, slag rims, unreacted slag grains and cement clinkers. Therefore, to predict the effective mechanical properties, the volume fraction of each composite phase directly obtained from statistical nanoindentation is more representative than the weight percentage of each single type of hydration products derived by quantitative analysis like XRD and TGA. Regarding pores not observable by nanoindentation, their volume fraction was calculated based on the greyscale histogram of BSE images at different ages according to the procedures suggested by Kocaba et el. [8]. The pore volume fraction (determined by BSE) of at 7-days, 28-days, 90-days and 2-years was 2.88 %, 1.81%, 1.49% and 0.72%, respectively.

The effective elastic modulus tested by microindentation and calculated by the corresponding two-scale micromechanical model are shown in the Fig. 12. In the microindentation test, the effective modulus increases by 3.12 GPa in Stage I (7-days to 28-days) and by 0.54 GPa in Stage II (28-days to 90-days). During Stage III (90-days to 2-years), a significant increase of 8.76 GPa is found. The results of the two-scale model show a reasonable agreement with the microindentation tests, especially at 2-years. However, before 90-days, the two-scale model overestimates the effective elastic modulus. To explain the difference between the two-scale model and microindentation results, this study proposes a hypothesis of interface between the slag grains and cement matrix, which will be explained in detailed in Section 4.2.

4. Discussion

4.1. The evolution process of HVSC from a chemo-micromechanical point of view

As mentioned above, published studies focus either on chemical or micromechanical aspects of slag cement paste, resulting in a lack of synergy between them. In the current study, we combined the chemical and micromechanical characterizations, and discuss the evolution process of HVSC at different periods as follows:

1) During Stage I (7-days to 28-days), a significant increase in C–S(A)–H gel phase content is observed (Fig. 5), which mainly results from the continuous hydration of cement clinkers and slag particles with small diameters [53,54]. The produced gel phase fills the pores, especially medium and large capillary pores, leading to a considerable reduction in porosity, as reflected in Figs. 9-10. Consequently, an increase in the effective elastic modulus of microindentation result is noted (Fig. 12), due to the densification of cement matrix.

2) During Stage II (28-days to 90-days), few changes are detected in the evolution of phase assemblage (Figs. 5 and 6) and microstructure development (Figs. 8 and 9). As a result, the microindentation results remain stable during this period, fluctuating at around 22.0 GPa. After 28-day curing, most cement clinkers have completely hydrated. Additionally, owing to its latent hydraulic property, slag particles, especially large ones, hydrate slowly [8,54], thus barely contributing to the improvement of various properties of HVSC paste. On the other hand, the peaks of LD-SCH and HD C-S-H coincide at this period (Fig. 10(c)), which indicates the transformation from LD C-S-H to HD C-S-H.

3) During Stage III (90-day to 2-year), the influence of slag (or pozzolanic reaction) increases. The continuous hydration of slag grains, especially large ones, generates large amount of hydrotalcite-like phase, as verified by XRD (Fig. 6) and EDS (Fig. 7(b)). This phase precipitates with C–S(A)–H gel phase closely, forming the so-called slag rim. As shown in Fig. 8(d), slag rims become much thicker after 2 years than that

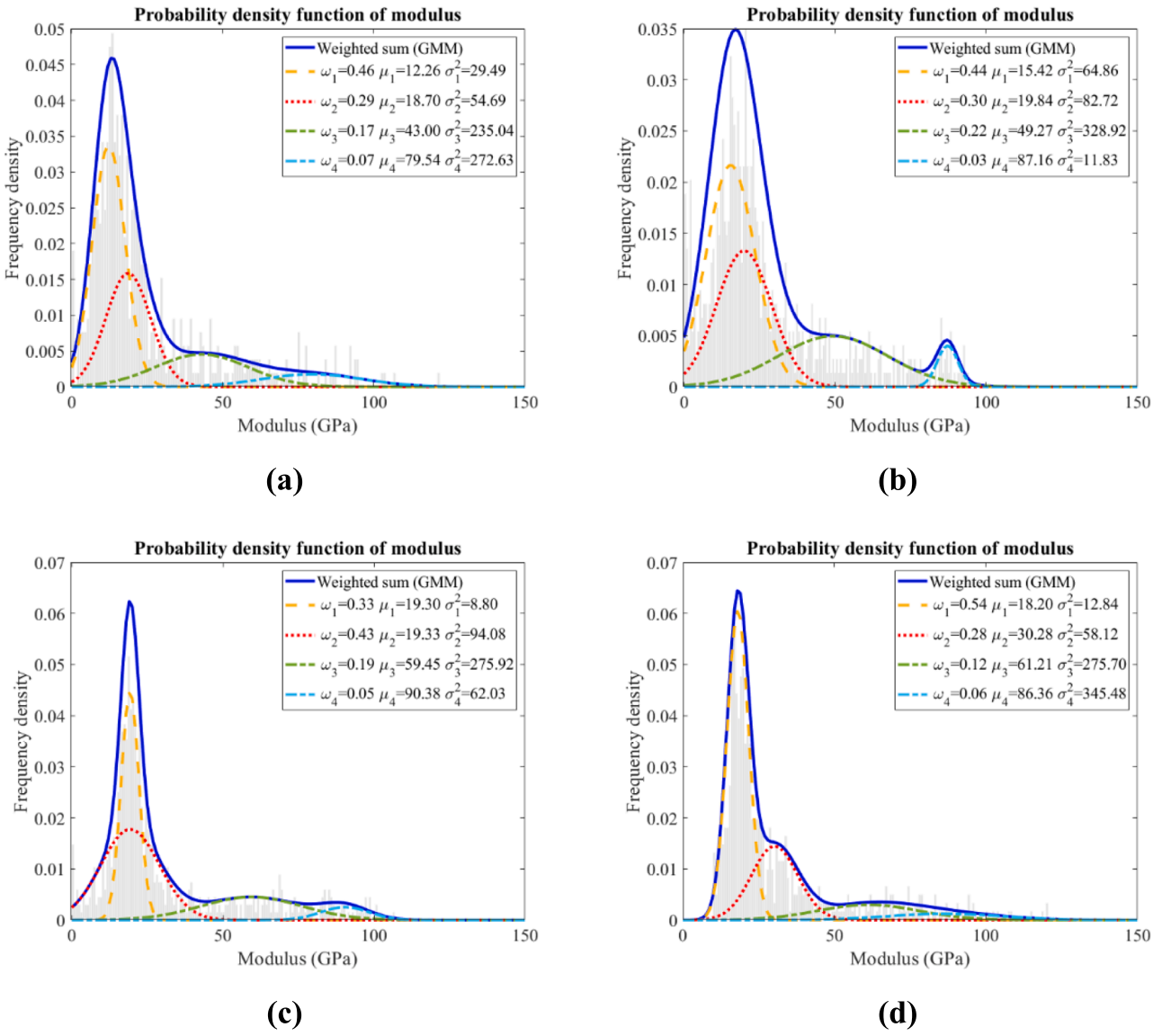

Fig. 11. Histogram and deconvolution results of elastic modulus measured by nanoindentation tests: a, b, c, d correspond to the HVSC samples tested at 7-day, 28-day, 90-day, and 2-year.

Table 2
The four (mixed) phases of HVSC sample distinguished by microindentation results at each sampling age.

	7-day	28-day	90-day	2-year
Phase 1	Pore, LD C-S-H	Pore, LD C-S-H	Pore, HD C-S-H	HD C-S-H
Phase 2	HD C-S-H	HD C-S-H	HD C-S-H, Slag-rim	HD C-S-H, Slag-rim
Phase 3	CH, Slag	CH, Slag	Slag, CH, Slag-rim	Slag, CH, Slag-rim
Phase 4	Slag, Clinker	Slag, Clinker	Slag, Clinker	Slag, Clinker

at 3 months (Fig. 8(c)).

Fig. 13 (a) and (b) show the greyscale value histograms of BSE images shown in Fig. 8 (b) and (d), representing HVSC paste samples at 28 days and 2 years, respectively. With the advancing of slag hydration, the slag rim thickens, and it occurs as an evident peak in the greyscale value histogram in Fig. 13 (b), before the main peak corresponding to the C–S(A)–H gel phase due to its low mean atomic number in composition (rich in Magnesium and Aluminum) [55]. As a result, the shoulder following the main Gaussian peak in the frequency plot of Fig. 13(d) is believed to belong to the slag rim, similar to the results obtained in our previous study [7].

4) Furthermore, a significant reduction in porosity is found during Stage III. The percentage of capillary pores keep decreasing, while the percentage of gel pores increases. Because of their relatively high mobility, Ca and Si ions dissolved from slag move into the cement matrix and precipitate into C − S(A) − H gel phase [11,56], resulting in the further refinement of microstructure of HVSC paste. Therefore, due to a combined effect of these beneficial microstructural changes, a much higher elastic modulus is measured after 2 years in the microindentation test (Fig. 13). A similar trend has been observed in a 40-year-old CEM III/B specimen investigated in our previous study [7]): After decades (e.g., sample (CEM III/B) of around 40-year-old investigated in our previous study [7]), the situation of HVSC sample is similar to that in Stage III examined in the present paper with reactive slag. As shown in [7], the slag rims were quite thick, and hydrotalcite-like phase dominated after such a long service life. The indentation modulus of slag rim was 35.55 ± 12.33 GPa in the 40-year-old sample, which is close to the value

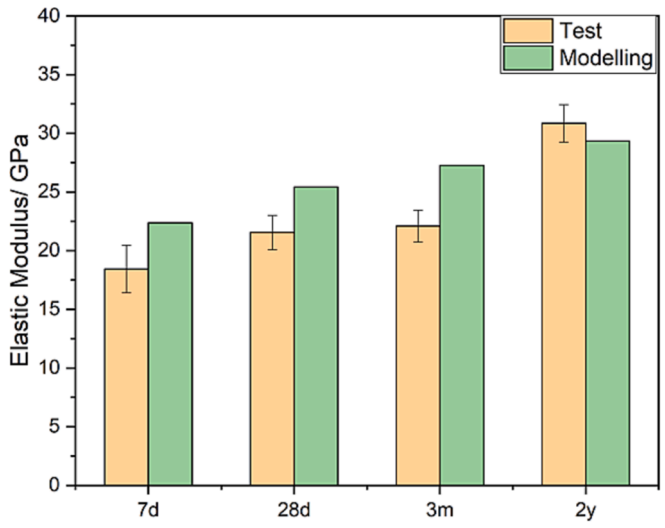

Fig. 12. Microindentation and modelling results of HVSC samples tested at 7-day, 28-day, 90-day, and 2-year.

determined herein for the 2-year HVSC paste (see Fig. 10(d)).

In general, published studies of slag cement pastes are limited to 28-day cured samples, up to several months at most. It has been long believed that this was sufficiently representative for slag cement paste and concrete. However, based on the results obtained herein, the beneficial potential of slag (or pozzolanic reaction) is underestimated by such (short-term) investigations. Although small slag grains almost hydrate totally before 3 months and contribute to the reduction of porosity, the hydration degree of slag only reaches ~30% within this time scale [57,58]. Based on BSE image analysis method proposed in [8], the hydration degree of slag increased from ~10.5% at 7 days to ~43.2% after 2 years. It also explains that for existing researches attempting to investigate the micro-mechanical properties of slag cement paste, only C–S–H gel phase, portlandite, unreacted slag particle and cement clinker are identified [19,59,60]. No information regarding slag rim is found before.

With prolonged curing, large slag grains further hydrate, and the slag rim emerges as an important component of the microstructure. On the one hand, Ca and Si dissolved from slag move into cement matrix and precipitate into the formation of C–S(A)–H gel phase, which decreases the porosity of the cement matrix. On the other hand, much more hydrotalcite-like phase is generated and precipitated in the slag rim, and thus a new component, i.e., the slag rim with a higher elastic modulus compared to the C–S(A)–H gel phase, starts to form. This contributes significantly to the enhanced micromechanical performance of slag-rich cement paste and concrete at later age.

4.2. *A hypothesis on the interface between unhydrated slag and C-A-S-H gel*

Before 90-days, large slag particles mainly serve as solid inclusions in the HVSC pastes due to their low-reactivity [53,54]. Note that the elastic modulus of unreacted slag grain typically reaches 81–115 GPa [22]. In Stage III (90-days to 2-years), a considerable amount of slag grains hydrates and thick rims are formed around them, whose elastic modulus is significantly lower (i.e., ~30 GPa shown in Fig. 11(d) and [7], versus 81–115 GPa for unreacted slag grains). Following the basic ideas of micromechanics (see Eq. (5–10)), the decrease of volume fraction of a solid inclusion (i.e., slag) should lead to the reduction of the effective elastic modulus of HVSC composite accordingly; however, this is not in agreement with the results of microindentation tests. This may be caused by the interface between the large unhydrated slag grains and the hydrated cement matrix. The formation of such interface is shown in Fig. 14(a), adapted from [61]. Števula et al. [61] confirmed that, after one year, hydration products at the interface mainly comprised needle-like ettringite, acicular C–S(A)–H gel, and portlandite crystals, which are considered to typically precipitate in large pores. These hydration products are found at the interface of concrete between (normal) aggregates and the cement matrix [62]. As shown in Fig. 14(a), these hydration products precipitated in the interface between large unhydrated slag particles and hydrated cement matrix indicate that this area is porous and that the bond is weak, which might compromise the overall stiffness of the HVSC composite. At later age (years) with the continuous hydration of slag particles, Ca and Si dissolved from slag move out and precipitate as C–S(A)–H gel phase in this porous area, the bond becomes denser and therefore increases the overall stiffness of HVSC composite, as shown by the microindentation result of the two-year HVSC paste (This process is illustrated in Fig. 14(b).).

In the two-scale micromechanical model, a perfect bond between all phases is assumed and the interface between the large unhydrated slag particles and the hydrated cement matrix is not explicitly considered. Before 90 days, when a weak porous bond exists in the interface between slag and hydrated cement, the model overestimates the effective elastic modulus of the HVSC composites due to the (inappropriate) assumption of the perfect bond. On the other hand, after 2 years, when large slag grains have hydrated to a certain extent, dissolved Ca and Si move out and precipitate as C–S(A)–H gel phase in this weak area, fill pores and thus strengthen the bond. Under this circumstance, the assumption of a perfect bond is valid, and the model show a good match with the microindentation tests. Overall, the model used herein is in reasonable agreement with the microindentation tests (see Fig. 12). An important reason for the good prediction is the stiffness-dependent phase identification based on statistical nanoindentation. In the statistical GMM analysis, the four mixed phases are identified and classified based only on the stiffness difference, irrespective of their different chemical

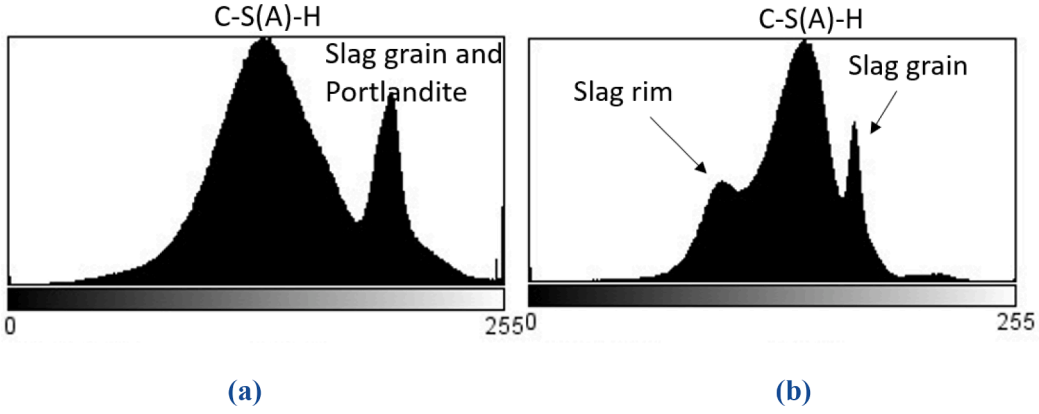

Fig. 13. (a) and (b) Grey value histograms of BSE images shown in Fig. 8 (b) and (d), respectively.

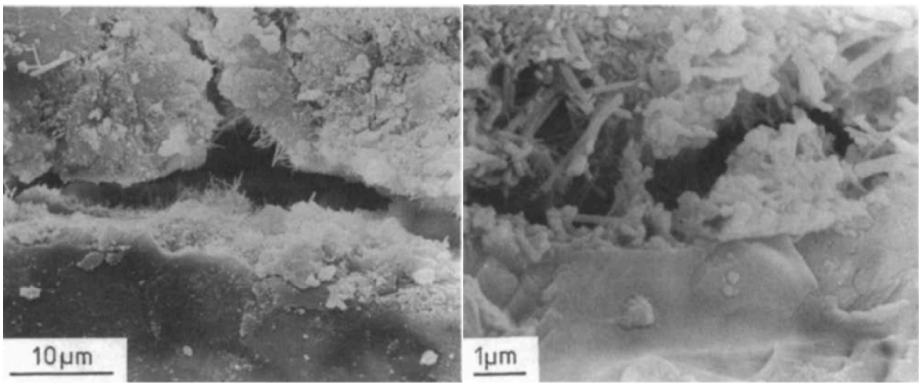

(a)

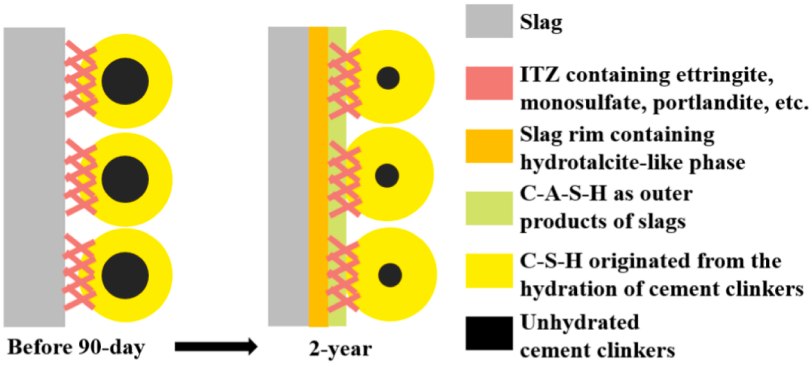

(b)

Fig. 14. Interface between unhydrated slag particle and hydrated cement matrix: (a) SEM images of the interface taken from [61]; (b) a schematic diagram of the evolution of interface.

compositions and microstructure. Therefore, the influence of imperfect bond is implicitly reflected by the micromechanical model, probably with a lower mean value of Phase 3 derived by statistical deconvolution analysis.

5. Conclusions

This study aims for the evolution process of the chemo-mechanical properties of HVSC specimens. TGA/ XRD/ MIP/ SEM-EDS tests and nanoindentation/ microindentation tests were conducted to characterize the evolution of phase assemblage and microstructure, as well as quantify the evolution of mechanical properties. Using statistical deconvolution results of the nanoindentation tests as input, a two-scale micromechanical model was used to predict the effective elastic modulus of the HVSC composites and compare the modelling results with microindentation tests. This study results in the following findings:

1) In Stage I (7-days to 28-days), hydration of cement clinkers dominates. The large generation of C-S-H gel phase fills medium and large capillary pores. Accordingly, an overall improvement in effective elastic modulus is observed due to the reduction in porosity.
2) In Stage II (28-days to 90-days), few changes are detected regarding the evolution of phase assemblage and microstructure of HVSC pastes. As a result, the effective elastic modulus tested by microindentation also remains stable. However, nanoindentation results show a transformation from LD C-S-H to HD C-S-H during this period.
3) In Stage III (90-days to 2-years), various characterization methods identify a significant increment of hydrotalcite-like phase, along with dark rims formed around large unreacted slag grains. As a result, a "new Phase 2" is identified in the statistical nanoindentation tests of 2-year-old paste, comprising mainly the slag rim. Furthermore, the microindentation tests shows a significant improvement of effective elastic modulus at this age.
4) The two-scale micromechanical model, based on SC scheme at level one and M−T at level two, can predict the effective modulus of HVSC composites with good accuracy, given the input of statistical nanoindentation tests. Nevertheless, the existence of large unhydrated slag grains-hydrated cement matrix interface may cause an overestimation of the calculated elastic moduli. With longer curing age, this interface disappears owing to the precipitation of C-A-S-H gel phase, originated from the hydration of large slag particles. Consequently, a better match is found between the modelling and experimental results at later ages.

CRediT authorship contribution statement

Minfei Liang: Conceptualization, Methodology, Formal analysis, Investigation, Data curation, Writing – original draft, Writing – review & editing. **Yu Zhang:** Conceptualization, Methodology, Formal analysis, Investigation, Data curation, Writing – original draft, Writing – review & editing. **Shan He:** Investigation, Writing – review & editing. **Yu Chen:** Investigation, Writing – review & editing. **Erik Schlangen:** Supervision, Funding acquisition, Writing – review & editing. **Branko Šavija:** Supervision, Funding acquisition, Writing – review & editing.

Declaration of Competing Interest

The authors declare that they have no known competing financial interests or personal relationships that could have appeared to influence the work reported in this paper.

Data availability

Data will be made available on request.

Acknowledgements

Minfei Liang would like to acknowledge the funding supported by China Scholarship Council under grant number 202007000027. Branko Šavija acknowledges the financial support of the European Research Council (ERC) within the framework of the ERC Starting Grant Project "Auxetic Cementitious Composites by 3D printing (ACC-3D)", Grant Agreement Number 101041342.

References

[1] J.S. Damtoft, J. Lukasik, D. Herfort, D. Sorrentino, E.M. Gartner, Sustainable development and climate change initiatives, Cem. Concr. Res. 38 (2008) 115–127, https://doi.org/10.1016/J.CEMCONRES.2007.09.008.
[2] Y. Li, Y. Liu, X. Gong, Z. Nie, S. Cui, Z. Wang, W. Chen, Environmental impact analysis of blast furnace slag applied to ordinary Portland cement production, J. Clean. Prod. 120 (2016) 221–230, https://doi.org/10.1016/j.jclepro.2015.12.071.
[3] J. Bijen, Benefits of slag and fly ash, Constr. Build. Mater. 10 (1996) 309–314, https://doi.org/10.1016/0950-0618(95)00014-3.
[4] A.M. Rashad, An overview on rheology, mechanical properties and durability of high-volume slag used as a cement replacement in paste, mortar and concrete, Constr. Build. Mater. 187 (2018) 89–117, https://doi.org/10.1016/j.conbuildmat.2018.07.150.
[5] Y., K.R. and L.H. Yang, Ironmaking, in Treatise on process metallurgy., in: Elsevier, 2014.
[6] W. Chen, H.J.H. Brouwers, The hydration of slag, part 2: reaction models for blended cement, J. Mater. Sci. 42 (2007) 444–464, https://doi.org/10.1007/s10853-006-0874-1.
[7] Y. Zhang, M. Liang, Y. Gan, O. Çopuroğlu, Micro-mechanical properties of slag rim formed in cement-slag system evaluated by nanoindentation combined with SEM, Materials. 15 (2022) 6347, https://doi.org/10.3390/ma15186347.
[8] V. Kocaba, E. Gallucci, K.L. Scrivener, Methods for determination of degree of reaction of slag in blended cement pastes, Cem. Concr. Res. 42 (2012) 511–525, https://doi.org/10.1016/J.CEMCONRES.2011.11.010.
[9] H. Ye, Nanoscale attraction between calcium-aluminosilicate-hydrate and Mg-Al layered double hydroxides in alkali-activated slag, Mater Charact 140 (2018) 95–102, https://doi.org/10.1016/j.matchar.2018.03.049.
[10] R. Taylor, I.G. Richardson, R.M.D. Brydson, Composition and microstructure of 20-year-old ordinary Portland cement–ground granulated blast-furnace slag blends containing 0 to 100% slag, Cem. Concr. Res. 40 (2010) 971–983, https://doi.org/10.1016/J.CEMCONRES.2010.02.012.
[11] B. Li, Q. Li, W. Chen, Spatial zonation of a hydrotalcite-like phase in the inner product of slag: new insights into the hydration mechanism, Cem. Concr. Res. 145 (2021), 106460, https://doi.org/10.1016/j.cemconres.2021.106460.
[12] K. Scrivener, R. Snellings, B. Lothenbach, A practical guide to microstructural analysis of cementitious materials, n.d.
[13] J.I. Escalante-Garcia, J.H. Sharp, The chemical composition and microstructure of hydration products in blended cements, Cem. Concr. Compos. 26 (2004) 967–976, https://doi.org/10.1016/j.cemconcomp.2004.02.036.
[14] A. Darquennes, B. Espion, S. Staquet, How to assess the hydration of slag cement concretes? Constr. Build. Mater. 40 (2013) 1012–1020, https://doi.org/10.1016/j.conbuildmat.2012.09.087.
[15] Y. Zhang, S. Zhang, Y. Chen, O. Çopuroğlu, The effect of slag chemistry on the reactivity of synthetic and commercial slags, Constr. Build. Mater. 335 (2022), 127493, https://doi.org/10.1016/J.CONBUILDMAT.2022.127493.
[16] Y. Zhang, Z. Wan, L.M. de Lima Junior, O. Çopuroğlu, Early age hydration of model slag cement: interaction among C3S, gypsum and slag with different Al2O3 contents, Cem. Concr. Res. 161 (2022), 106954, https://doi.org/10.1016/j.cemconres.2022.106954.
[17] Y. Zhang, E. Schlangen, O. Çopuroğlu, Effect of slags of different origins and the role of sulfur in slag on the hydration characteristics of cement-slag systems, Constr. Build. Mater. 316 (2022), 125266, https://doi.org/10.1016/j.conbuildmat.2021.125266.
[18] G. Constantinides, F.J. Ulm, The effect of two types of C-S-H on the elasticity of cement-based materials: results from nanoindentation and micromechanical modeling, Cem. Concr. Res. 34 (2004) 67–80, https://doi.org/10.1016/S0008-8846(03)00230-8.
[19] C. Hu, Z. Li, Y. Gao, Y. Han, Y. Zhang, Investigation on microstructures of cementitious composites incorporating slag, Adv. Cem. Res. 26 (2014) 222–232, https://doi.org/10.1680/adcr.13.00029.
[20] E. Schlangen, E.J. Garboczi, Fracture simulations of concrete using lattice models: computational aspects, Eng. Fract. Mech. 57 (1997) 319–332, https://doi.org/10.1016/S0013-7944(97)00010-6.
[21] O. Bernard, F.-J. Ulm, E. Lemarchand, A multiscale micromechanics-hydration model for the early-age elastic properties of cement-based materials, Cem. Concr. Res. 33 (2003) 1293–1309, https://doi.org/10.1016/S0008-8846(03)00039-5.
[22] Y. Wei, X. Gao, S. Liang, Nanoindentation-based study of the micro-mechanical properties, structure, and hydration degree of slag-blended cementitious materials, J. Mater. Sci. 51 (2016) 3349–3361, https://doi.org/10.1007/s10853-015-9650-4.
[23] B. Šavija, H. Zhang, E. Schlangen, Micromechanical testing and modelling of blast furnace slag cement pastes, Constr. Build. Mater. 239 (2020) 117841.
[24] J. Zhang, G.W. Scherer, Comparison of methods for arresting hydration of cement, Cem. Concr. Res. 41 (2011) 1024–1036, https://doi.org/10.1016/J.CEMCONRES.2011.06.003.
[25] R. Kumar, B. Bhattacharjee, Study on some factors affecting the results in the use of MIP method in concrete research, Cem. Concr. Res. 33 (2003) 417–424, https://doi.org/10.1016/S0008-8846(02)00974-2.
[26] M. Miller, C. Bobko, M. Vandamme, F.J. Ulm, Surface roughness criteria for cement paste nanoindentation, Cem. Concr. Res. 38 (2008) 467–476, https://doi.org/10.1016/J.CEMCONRES.2007.11.014.
[27] P.S. Phani, W.C. Oliver, G.M. Pharr, On the effective load during nanoindentation creep testing with continuous stiffness measurement (CSM), J. Mater. Res. 36 (8) (2021) 1740–1750.
[28] W.C. Oliver, G.M. Pharr, An improved technique for determining hardness and elastic modulus using load and displacement sensing indentation experiments, J. Mater. Res. 7 (1992) 1564–1583, https://doi.org/10.1557/jmr.1992.1564.
[29] C. Hu, Z. Li, A review on the mechanical properties of cement-based materials measured by nanoindentation, Constr. Build. Mater. 90 (2015) 80–90, https://doi.org/10.1016/j.conbuildmat.2015.05.008.
[30] D. Davydov, M. Jirásek, L. Kopecký, Critical aspects of nano-indentation technique in application to hardened cement paste, Cem. Concr. Res. 41 (2011) 20–29, https://doi.org/10.1016/J.CEMCONRES.2010.09.001.
[31] Z. Hu, M. Wyrzykowski, M. Griffa, K. Scrivener, P. Lura, Young's modulus and creep of calcium-silicate-hydrate compacts measured by microindentation, Cem. Concr. Res. 134 (2020) 106104.
[32] A simple theory of static and dynamic hardness, Proc. R. Soc. Lond. A Math. Phys. Sci. 192 (1948). doi: 10.1098/rspa.1948.0008.
[33] G.M. Pharr, A. Bolshakov, Understanding nanoindentation unloading curves, J. Mater. Res. 17 (10) (2002) 2660–2671.
[34] G. Constantinides, F.-J. Ulm, The elastic properties of calcium-leached cement pastes and mortars: A multi-scale investigation, n.d.
[35] F.J. Ulm, M. Vandamme, H.M. Jennings, J. Vanzo, M. Bentivegna, K.J. Krakowiak, G. Constantinides, C.P. Bobko, K.J. van Vliet, Does microstructure matter for statistical nanoindentation techniques? Cem. Concr. Compos. 32 (2010) 92–99, https://doi.org/10.1016/J.CEMCONCOMP.2009.08.007.
[36] C. Hu, Y. Gao, Y. Zhang, Z. Li, Statistical nanoindentation technique in application to hardened cement pastes: influences of material microstructure and analysis method, Constr. Build. Mater. 113 (2016) 306–316, https://doi.org/10.1016/j.conbuildmat.2016.03.064.
[37] T. Mori, K. Tanaka, Average stress in matrix and average elastic energy of materials with misfitting inclusions, Acta Metall. 21 (1973) 571–574, https://doi.org/10.1016/0001-6160(73)90064-3.
[38] R. Hill, A self-consistent mechanics of composite materials, J. Mech. Phys. Solids 13 (1965) 213–222, https://doi.org/10.1016/0022-5096(65)90010-4.
[39] X. Gao, Y. Wei, W. Huang, Effect of individual phases on multiscale modeling mechanical properties of hardened cement paste, Constr. Build. Mater. 153 (2017) 25–35, https://doi.org/10.1016/j.conbuildmat.2017.07.074.
[40] C. Hu, Z. Li, Micromechanical investigation of Portland cement paste, Constr. Build. Mater. 71 (2014) 44–52, https://doi.org/10.1016/j.conbuildmat.2014.08.017.
[41] S. Liang, Y. Wei, Z. Wu, Multiscale modeling elastic properties of cement-based materials considering imperfect interface effect, Constr. Build. Mater. 154 (2017) 567–579, https://doi.org/10.1016/j.conbuildmat.2017.07.196.
[42] J. Qu, M. Cherkaoui, Fundamentals of Micromechanics of Solidss, 2007. doi: 10.1002/9780470117835.
[43] J.T. Kloprogge, J. Kristóf, R.L. Frost, Thermogravimetric analysis-mass spectrometry (TGA-MS) of hydrotalcites containing CO32−, NO3−, Cl−, SO42− or ClO4−, in: 2001. A Clay Odyssey, Elsevier, 2003: pp. 451–458. doi: 10.1016/B978-044450945-1/50147-0.
[44] J.C.A.A. Roelofs, J.A. van Bokhoven, A.J. van Dillen, J.W. Geus, K.P. de Jong, The thermal decomposition of Mg-Al hydrotalcites: effects of interlayer anions and characteristics of the final structure, Chem. A Eur. J. 8 (2002) 5571–5579, https://doi.org/10.1002/1521-3765(20021216)8:24<5571::AID-CHEM5571>3.0.CO;2-R.
[45] I.G. Richardson, Tobermorite/jennite- and tobermorite/calcium hydroxide-based models for the structure of C-S-H: applicability to hardened pastes of tricalcium silicate, β-dicalcium silicate, Portland cement, and blends of Portland cement with blast-furnace slag, metakaolin, or silica fume, Cem. Concr. Res. 34 (2004) 1733–1777, https://doi.org/10.1016/j.cemconres.2004.05.034.
[46] F. Deschner, F. Winnefeld, B. Lothenbach, S. Seufert, P. Schwesig, S. Dittrich, F. Goetz-Neunhoeffer, J. Neubauer, Hydration of Portland cement with high replacement by siliceous fly ash, Cem. Concr. Res. 42 (2012) 1389–1400, https://doi.org/10.1016/j.cemconres.2012.06.009.
[47] S.M. J.F. Young, Concrete Prentice-Hall, 1981.

[48] P.D. Tennis, H.M. Jennings, A model for two types of calcium silicate hydrate in the microstructure of Portland cement pastes, Cem. Concr. Res. 30 (2000) 855–863, https://doi.org/10.1016/S0008-8846(00)00257-X.
[49] Z. Luo, W. Li, Y. Gan, X. He, A. Castel, D. Sheng, Nanoindentation on micromechanical properties and microstructure of geopolymer with nano-SiO2 and nano-TiO2, Cem. Concr. Compos. 117 (2021), https://doi.org/10.1016/j.cemconcomp.2020.103883.
[50] Y. He, S. Liu, X. Zhang, W. Liu, G. Liao, M. Xu, Influence of triethanolamine on mechanical strength and hydration performance of blended cement containing fly ash, limestone and slag, J. Build. Eng. 44 (2021) 102879.
[51] J. Baronet, L. Sorelli, J.-P. Charron, M. Vandamme, J. Sanahuja, A two-scale method to rapidly characterize the logarithmic basic creep of concrete by coupling microindentation and uniaxial compression creep test, Cem. Concr. Compos. 125 (2022) 104274.
[52] P. Suwanmaneechot, A. Aili, I. Maruyama, Creep behavior of C-S-H under different drying relative humidities: interpretation of microindentation tests and sorption measurements by multi-scale analysis, Cem. Concr. Res. 132 (2020) 106036.
[53] J. Zhu, Q. Zhong, G. Chen, D. Li, Effect of particlesize of blast furnace slag on properties of portland cement, Procedia Eng. 27 (2012) 231–236, https://doi.org/10.1016/j.proeng.2011.12.448.
[54] P.Z. Wang, R. Trettin, V. Rudert, Effect of fineness and particle size distribution of granulated blast-furnace slag on the hydraulic reactivity in cement systems, Adv. Cem. Res. 17 (2005) 161–167, https://doi.org/10.1680/adcr.2005.17.4.161.
[55] S. Miyata, Physico-chemical properties of synthetic hydrotalcites in relation to composition, Clays Clay Miner. 28 (1980) 50–56, https://doi.org/10.1346/CCMN.1980.0280107.
[56] Y. Zhang, O. Çopuroğlu, The role of hydrotalcite-like phase and monosulfate in slag cement paste during atmospheric and accelerated carbonation, Cem. Concr. Compos. 132 (2022), 104642, https://doi.org/10.1016/j.cemconcomp.2022.104642.
[57] J.S. Lumley, R.S. Gollop, G.K. Moir, H.F.W. Taylor, Degrees of reaction of the slag in some blends with Portland cements, Cem. Concr. Res. 26 (1996) 139–151, https://doi.org/10.1016/0008-8846(95)00190-5.
[58] K. Luke, F.P. Glasser, Selective dissolution of hydrated blast furnace slag cements, Cem. Concr. Res. 17 (1987) 273–282, https://doi.org/10.1016/0008-8846(87)90110-4.
[59] V. Zanjani Zadeh, C.P. Bobko, Nanoscale mechanical properties of concrete containing blast furnace slag and fly ash before and after thermal damage, Cem. Concr. Compos. 37 (2013) 215–221, https://doi.org/10.1016/j.cemconcomp.2012.09.003.
[60] Z. He, C. Qian, Y. Zhang, F. Zhao, Y. Hu, Nanoindentation characteristics of cement with different mineral admixtures, Sci. China Technol. Sci. 56 (2013) 1119–1123, https://doi.org/10.1007/s11431-013-5186-5.
[61] L. Ŝtevula, J. Madej, J. Kozánková, J. Madejová, Hydration products at the blastfurnace slag aggregate – cement paste interface, Cem. Concr. Res. 24 (1994) 413–423, https://doi.org/10.1016/0008-8846(94)90128-7.
[62] K.L. Scrivener, A.K. Crumbie, P. Laugesen, The Interfacial Transition Zone (ITZ) between cement paste and aggregate in concrete, Interface Sci. 12 (2004) 411–421, https://doi.org/10.1023/B:INTS.0000042339.92990.4c.